Magnetic-thermal external field activate the pyro-magnetic effect of pyroelectric crystal (NaNbO$_3$) to build a promising multi-field coupling-assisted photoelectrochemical water splitting system

Tianhao Li [a,b], Yongjin Zou [c,*], Zhifeng Liu [a,b,**]

[a] School of Materials Science and Engineering, Tianjin Chengjian University, 300384 Tianjin, China
[b] Tianjin Key Laboratory of Building Green Functional Materials, 300384 Tianjin, China
[c] Guangxi Key Laboratory of Information Materials, Guilin University of Electronic Technology, 541004 Guilin, China

ARTICLE INFO

ABSTRACT

Rationalizing the external field advantage and manipulating more carrier separation is of great significance for expanding the research of external field-assisted photoelectrochemical (PEC) water splitting. Hence, we choose NaNbO$_3$ material with pyroelectric properties for the realization of an efficient multi-field coupled-assisted PEC water splitting system using magnetic and temperature fields for the first time. Detailed experimental results show that the enhancement of photoelectric performance by magnetic fields seems to be limited. However, it is amazing that the coupling effect of magnetic and thermal field triggers the generation of pyro-magnetic effect, which breaks the limitation of non-radiative recombination of magnetic field manipulated carriers, and significantly improves the performance of PEC water splitting. The multi-field coupling drive the current density of the photoanode to span to 0.45 mA at 1.23 V vs. RHE (3 times higher than photocurrent). The first principle density functional theory (DFT) calculation is combined with experimental tests to fundamentally understand the interrelationship between crystal structure changes, charge density distribution and external fields, and the effect on catalytic performance. This research provides insights into the interaction mechanism between external fields and the radiative/non-radiative recombination of manipulating carriers. Insights are provided for the establishment of a multi-field coupling-assisted PEC water splitting system.

1. Introduction

Nowadays, the global energy shortage and security have become the focus of attention. Developing clean and green sustainable energy is the key to solve the problem. The emergence of hydrogen energy is undoubtedly the best choice, and the fossil free preparation method is regarded as the cornerstone of cost saving and energy security. Photoelectrochemical (PEC) water splitting technology has unique advantages as a clean and renewable strategy for hydrogen production [1–6]. The application of semiconductor materials in PEC process is undoubtedly the most key protagonist. It carries the occurrence of key steps such as capturing light, separating and transferring excitation charges [7–9]. Therefore, researchers are committed to developing different types of semiconductor materials, from the beginning wide band gap semiconductors, such as TiO$_2$ and ZnO [10,11], to the subsequent

development of narrow band gap semiconductors: α-Fe$_2$O$_3$ [12,13], BiVO$_4$ [14,15], and CdS [16,17]. However, both wide band gap semiconductors and narrow band gap semiconductors have obvious defects in the practical application of PEC water splitting to produce hydrogen due to their own conditions. As a result, many modification strategies have emerged: doping, heterojunctions, co-catalysts and other strategies. However, the semiconductor still faces the problem of high carrier recombination efficiency. Therefore, there is an urgent need to develop more strategies to solve the above thorny problems.

In recent years, the external field assisted strategy is an effective approach. The recombination of manipulate carriers has been a hot topic and a key link in the process of external field assisted PEC water splitting. The underlying reason is that the external field can provide additional energy to the electrode system and drive more electron-hole pair separation through the unique properties of the material, which can

---

effectively improve the performance of PEC water splitting [18–22]. Semiconductor materials with non-centrosymmetric structures exhibit unique piezoelectric and pyroelectric properties under external field excitation, which can manipulate the recombination of electron hole pairs produced by illumination [23]. Recently, using the piezoelectric characteristics of ZnO, the recombination of carriers is successfully suppressed through the built-in electric field, which makes it have a good application in the field of PEC [24]. Similarly, pyroelectric materials can collect energy under natural temperature difference and use it to assist in photoelectrochemical water splitting. For instance, Qiao et al. used the pyroelectricity of bismuth tungstate (Bi_2WO_6) to improve its water decomposition efficiency under the natural temperature difference of 20–45 ℃ [25]. However, as a material with both semiconductor and pyroelectric properties, sodium niobate ($NaNbO_3$) is an excellent candidate with excellent nonlinear optical, ferroelectric, ionic conductivity, and photorefractive properties [26–30]. So far, You et al. have achieved the thermal catalytic decomposition performance of $NaNbO_3$ with different morphologies under the heating-cooling cycle of 23–50 ℃ [26]. In previous work, Zhang et al. also successfully constructed a pyroelectric assisted photoelectrochemical system for efficient decomposition of water [31]. Nevertheless, it is still difficult to manipulate the separation of more carriers and the efficiency of $NaNbO_3$ photoelectrode with external field assistance is still low, which does not reach a more ideal state.

For this reason, we propose a multi-field coupling-assisted PEC strategy to manipulate more carrier separation in order to obtain higher carrier separation efficiency and to better apply it to the PEC water splitting field. In many applications of external field energy at current stage, temperature and pressure can tally with the electrode system. In addition, as another non-contact radiation field, magnetic field can invisibly penetrate the whole electrode system, and its introduction into PEC water splitting process is a novel external field auxiliary strategy [32]. For example, Yang et al. successfully introduced magnetic fields into different types of semiconductor PEC water splitting processes to enhance their photoelectric performance [32]. However, the effect provided by a single magnetic field may be limited or weak for the performance enhancement of PEC water splitting. Thus, multi-field coupling to assist PEC water splitting provides an opportunity for the development of semiconductor materials with unique properties. At present, there are few studies on the coupling of multiple external fields. The mechanism of influence between external fields is not clear, and the specific catalytic processes need to be explored. Moreover, the magnetic field is an advantageous selection in the multi-field coupling-assisted PEC water splitting, and the mechanism related between the magnetic field dynamics and charge transfer is not explained in sufficient detail. The theories related to spin polarization and magnetic field coupling need to be expanded. And, the reasons limiting the performance improvement are not yet clear.

As a result of integration of all the considerations mentioned above, we employed non-contact type external fields (magnetic and temperature fields) in this research, which can invisibly penetrate the whole PEC water splitting process, and successfully constructed a multi-field coupled-assisted PEC water splitting system for $NaNbO_3$ materials with pyroelectric properties for first time. Based on the successful construction of $NaNbO_3$ pyro-photo-electric catalysis system, we investigated the processes of magnetic field-assisted photoelectric and pyroelectric catalysis, respectively. In the process of exploration, we were amazed to find that the performance of magnetic field-assisted pyroelectric catalysis was significantly enhanced. It was found that the coupling effect of magnetic and thermal fields triggered the pyromagnetic effect, breaking the limitation of non-radiative recombination of magnetic field manipulated carriers. Meanwhile, density functional theory (DFT) is combined with experimental tests to fundamentally understand the interrelationship between crystal structure changes, charge density distribution and external fields, and the effect on catalytic performance. Subsequently, the feasibility of multi-field coupling-assisted PEC water splitting is proposed.

2. Experimental section

2.1. Synthesis of $NaNbO_3$ photoanode

We synthesized $NaNbO_3$ sample according to previous research reports [31]. Subsequently, the spin coating method is used to prepare the electrode film required for testing performance. In detail, we dispersed 50 mg of $NaNbO_3$ powder in 200 μL isopropyl alcohol, and add 100 μL binder to improve adhesion.

2.2. Characterization

We used dried powder samples for powder X-ray diffraction (XRD) and X-ray photoelectron spectroscopy (XPS) measurements. XRD patterns were recorded on a diffractometer (XRD, D/Max-2500, Rigaku) using Cu Kα radiation ($\lambda = 0.15418$ nm) to characterize the phase identification and crystal structure of the synthetic samples. The X-ray photoelectron spectroscopy (XPS) measurement uses Al Kα radiation (hν = 1486.6 eV) to record the spectrum on Thermo ESCALAB250XI system to characterize the composition and surface chemical state of synthetic elements. The surface morphologies and microstructures of the samples were characterized by a field emission-scanning electron microscope (FE-SEM, TESCAN MIRA LMS) and transmission electron microscopy (TEM), and high-resolution TEM images (HRTEM) measurements were carried by a Tecnai G2 20 transmission electron microscope. The elemental distribution and content of the synthesized materials were analyzed by energy dispersive spectrum (EDS, TESCAN MIRA LMS). In addition, we obtain the specific surface area of the material by BET (TriStar II 3flex) test. Absorption spectra were carried out using the UV–vis double-beam spectrophotometers (UV–vis, DU-8B). The incident photon-to-current efficiency (IPCE) was tested by the photoelectric chemistry test analysis system (CEL-SLF-Vertex).

2.3. Photoelectrochemical measurements

The photoelectrochemical performances of the photoelectrode is measured by a standard three-electrode system. The electrochemical workstation used is CHI760E (Chenhua, Shanghai, China). A solar simulator (CHF-XM500, 100 mW cm^{-2}) coupled with an air mass 1.5 G (AM 1.5 G) filter was employed as the light source. The measured potentials were converted against the reversible hydrogen electrode (RHE) using the Nernst equation [33].

$$E_{RHE} = E_{Ag/AgCl} + 0\cdot0591 \text{ pH} + 0\cdot1976 \text{ V} \quad (1)$$

The photocurrent-potential (I-V) curves were obtained by linear sweep voltammetry (LSV) with potential range from 0 V_{RHE} to 1.23 V_{RHE} at a scan rate of 0.01 V·s^{-1}. Electrochemical impedance spectroscopy (EIS) was analyzed at a scan rate of 20 mV/s using an AC amplitude of 5 mV and a frequency range of 100 kHz to 0.1 Hz.

3. Results and discussion

3.1. Structure characterization of $NaNbO_3$ electrodes

Firstly, the morphology of the prepared $NaNbO_3$ was revealed by FE-SEM (Fig. 1) and TEM (Fig. 2). As seen in Fig. 1a, the shape of $NaNbO_3$ is cube, the particle size is irregular, and its specific surface area (10.35 m^2/g) was determined by BET test. Furthermore, Fig. S1 shows the EDS spectrum of $NaNbO_3$, which possesses distinct characteristic peaks of Na, Nb and O elements. In addition, the elemental mapping (Fig. 1c-f) shows the spatial distribution of Na, Nb and O elements, and the uniform distribution of the three elements in the $NaNbO_3$ nanocube can be clearly observed. The boundary of the nanocube can be clearly observed
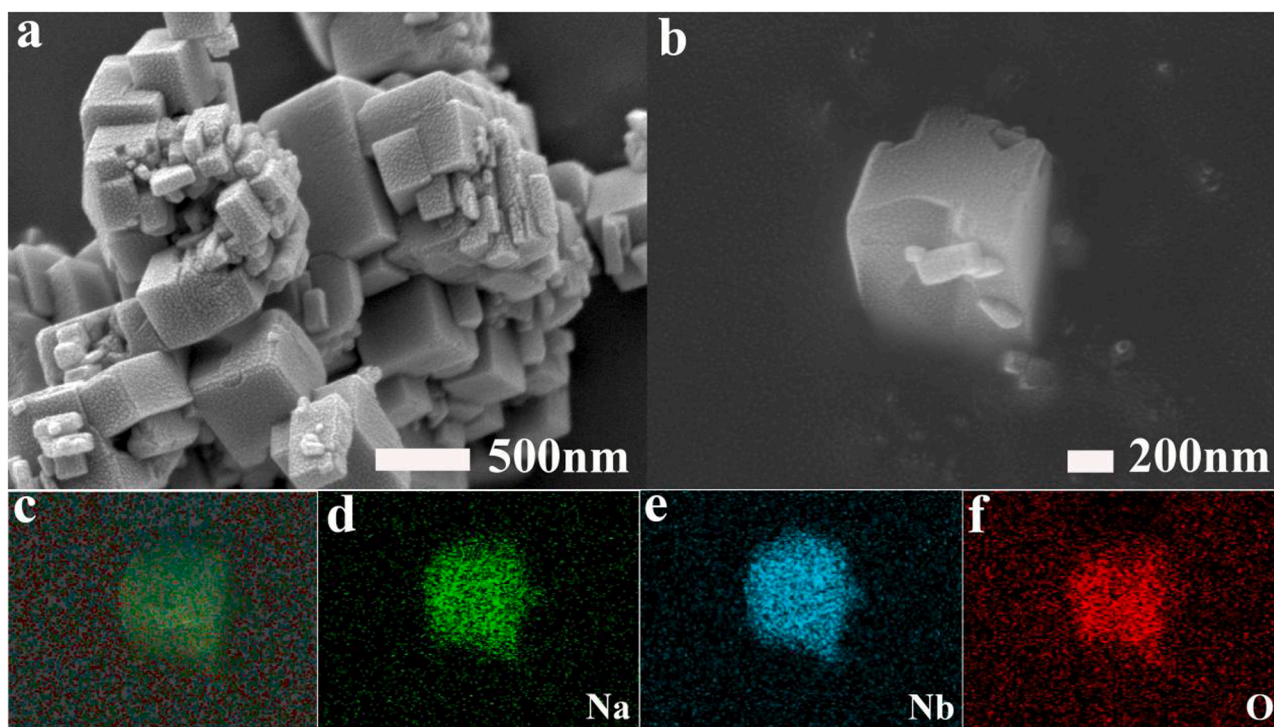
Fig. 1. (a, b) FE-SEM image of NaNbO$_3$; (c-f) EDX mapping images of NaNbO$_3$.
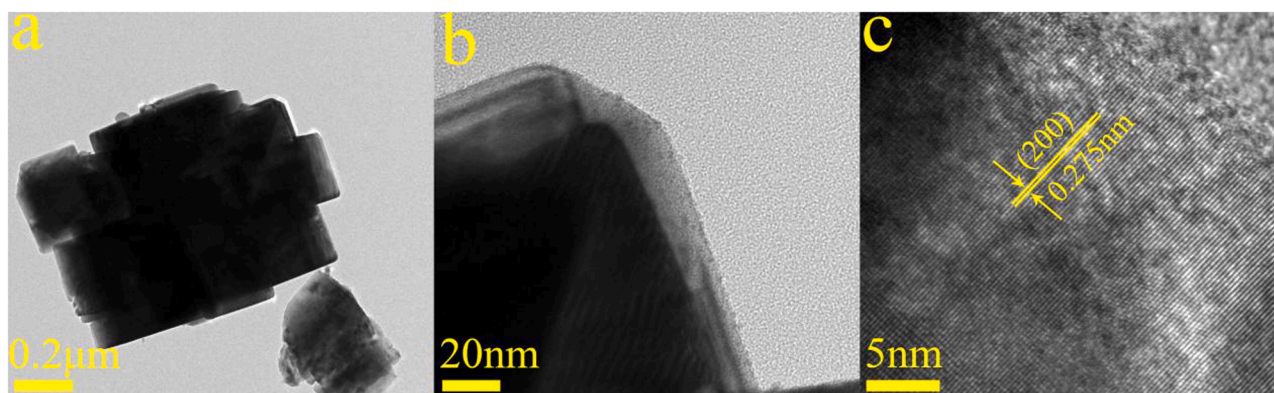

Fig. 2. (a, b) TEM and (c) HRTEM images of NaNbO$_3$.

from the TEM image (Fig. 2b). The high-resolution TEM (HRTEM) image in Fig. 2c is obtained from a randomly selected region of the nanocube, clearly showing the crystalline NaNbO$_3$ nanocube derived from continuous lattice fringes. The HRTEM image (Fig. 2c) clearly shows that the crystal plane spacing d is 0.275 nm, corresponding to the {200} plane, which further indicates the good crystallinity of NaNbO$_3$.

For the study of semiconductor materials, the crystal system and point group determine their internal structure and properties. Therefore, it is very important to study the crystal structure of NaNbO$_3$ before characterization. As shown in Fig. 3a, NaNbO$_3$ appears as an orthogonal crystal at room temperature [31]. However, different from other perovskite structures, the [NbO$_6$]$^-$ octahedron in NaNbO$_3$ structure is in an inclined state, which directly leads to different Nb-O bond lengths and angles. This makes the positive and negative charge centers do not coincide and show spontaneous polarization [34,35]. We further confirmed the crystal structure of the prepared NaNbO$_3$, and the XRD spectrum is shown in Fig. 3b. Obviously, all diffraction peaks correspond to the orthogonal phase NaNbO$_3$ (JCPDS 73–0803). Fig. 3c-d enlarges the positions of the first two main diffraction peaks, showing that there

are no other impurity peaks in the diffraction pattern.

Moreover, to further study the chemical state of each element in NaNbO$_3$, XPS measurement is shown in Fig. S2. The high-resolution spectrum of each element is shown in Fig. 4. Only one main peak of Na 1 s XPS spectrum is located at 1071.2 eV. It is worth noting that due to the Nb 3d5/2 and Nb 3d3/2 of pentavalent niobium, the high-resolution Nd 3d XPS spectrum has two main peaks, with centers at 206.7 eV and 209.4 eV and spin orbit splitting of 2.7 eV [36]. Moreover, the high symmetry of the peak and the narrow half peak width show that Nb^{5+} is monovalent. Interestingly, there is not only one peak in the O 1 s XPS spectrum, which indicates the coexistence of three forms of O. The main peak of O 1 s can be deconvoluted into two peaks with binding energies of 529.6 eV and 531.6 eV respectively. The former is attributed to lattice oxygen species (O^{2-}) and the latter is attributed to surface oxygen [37]. Finally, at the binding energy of 533.8 eV, there is a surface absorbed OH$^-$ group.
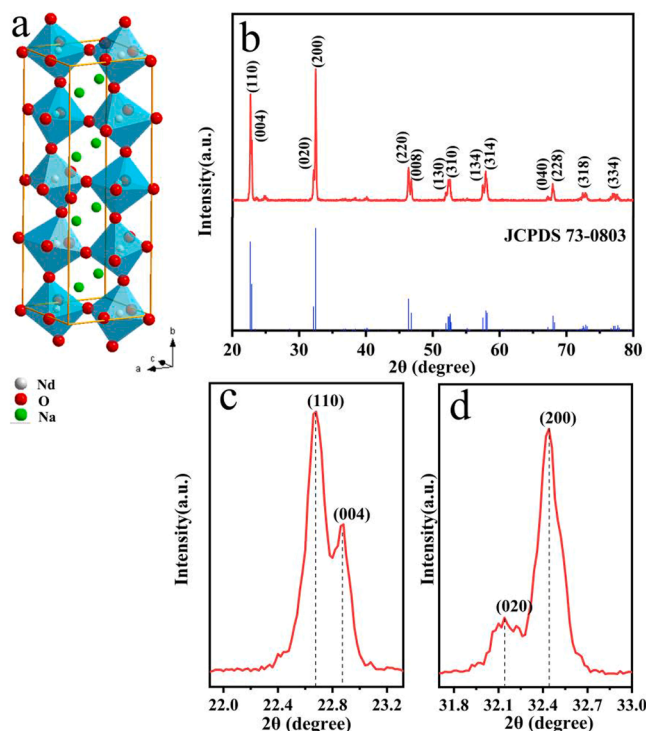
Fig. 3. (a) Schematic crystal structures of orthorhombic $NaNbO_3$; (b) XRD spectrum and (c-d) a portion of XRD spectrum of $NaNbO_3$.

3.2. Magnetic field assisted photoelectric catalysis of NaNbO₃ electrodes

As a kind of semiconductor material in PEC water splitting, the light harvesting capability is significant [38]. The UV-Vis absorption spectrum of $NaNbO_3$ is shown in Fig. S3. The absorption edge is about 366 nm, the corresponding bandgap energy is 3.38 eV. The magnetic field as a non-contact type external field is able to pass invisibly through the semiconductor material. Therefore, the external magnetic field is able to couple with the process of photoelectric catalysis. We use permanent magnets (5 cm × 5 cm × 2 cm, ~100 mT) to provide external magnetic field, and study the influence of magnetic pole and magnetic field direction in advance, as shown in Fig. S4. The magnetic pole has little effect on the photoelectrode. The relative position of the magnet and the photoelectrode has different effects on the performance. When the magnet and the photoelectrode are relatively parallel, the influence of Lorentz force is more significant [32,39,40]. In the following discussion, a magnet relatively parallel to the electrode is applied, and the schematic diagram of the photoelectric catalysis process with the assistance of the magnetic field is shown in Fig. S5. The samples were

sprayed on FTO as the working electrode, and platinum (Pt) and Ag/AgCl were used as the counter and reference electrodes, respectively. As shown in Fig. S6a, the measured I-V curves show an elevated current density value of 1.09 times through the magnetic field-assisted. The current density is 0.165 mA/cm^2 at 1.23 V_{RHE}. The regular elevation of photocurrent value may be caused by the influence of magnetic field on the thermodynamic process of photoelectrode in the water splitting. In this process, the most important section that should be concerned, besides the changes in the photo-absorption characteristics, is the separation and transport of photogenerated charges. For the photo-absorption characteristics, the inter band magneto-optical absorption phenomenon is only possible when the magnetic field strength is high, which in turn affects the photo-absorption characteristics of the semiconductor. When the applied magnetic field strength is weak, the Seeman energy generated by the magnetic field is not sufficient to change the photo-absorption of the semiconductor (as in Fig. S3). After excluding the influence of photo-absorption characteristics, we investigate the transportation and separation properties of photogenerated charges assisted by magnetic field by Mott-Schottky test. The calculation is based on the following equation: [41].

$$1/C^2 = (2/\varepsilon\varepsilon_0 e_0 A N_d)(V - V_{fb} - K_B T/e_0) \tag{2}$$

where C, ε and ε_0 is the space charge capacitance, relative permittivity of $NaNbO_3$ (290) and the permittivity of vacuum, A is coated electrode area (1 cm^2), N_d is donor density and e_0 is fundamental electron charge, T is the absolute temperature (in K), and K_B is Boltzmann constant (1.38×10^{-23} J K^{-1}), V is the electrode applied bias, respectively. The Mott-Schottky plot as in Fig. S6c shows a slight negative shift in V_{fb}, which indicates that the magnetic field has an effect on the charge transport at the electrode/electrolyte interface, which leads to an increase in the negative potential required to reach the flat-band state. In other words, the Lorentz force imparted to the moving charge by the magnetic field not only makes the Faraday charge transport slightly elevated, but also promotes the carrier transport at the electrode/electrolyte interface. In addition, from the photoelectroanalytical Bode phase analysis (Fig. S7c), it is also observed that under the effect of magnetic field, it shows a positive shift from the phase frequency peak to the high-frequency value, which also indicates that the charge transfer process of the electrode is accelerated. Subsequently, we explored its charge separation efficiency with the assistance of magnetic field by adding hole scavenger in the electrolyte solution. Before the test, the J_{abs} of electrodes was determined by calculation, and the detailed calculation process is presented in the Support Information. The charge-separation efficiency in the bulk (η_{bulk}) and on the surface ($\eta_{surface}$) was determined by the following equations: [42–44].

$$\eta_{bulk} = J_{Na2SO3}/J_{abs} \tag{3}$$

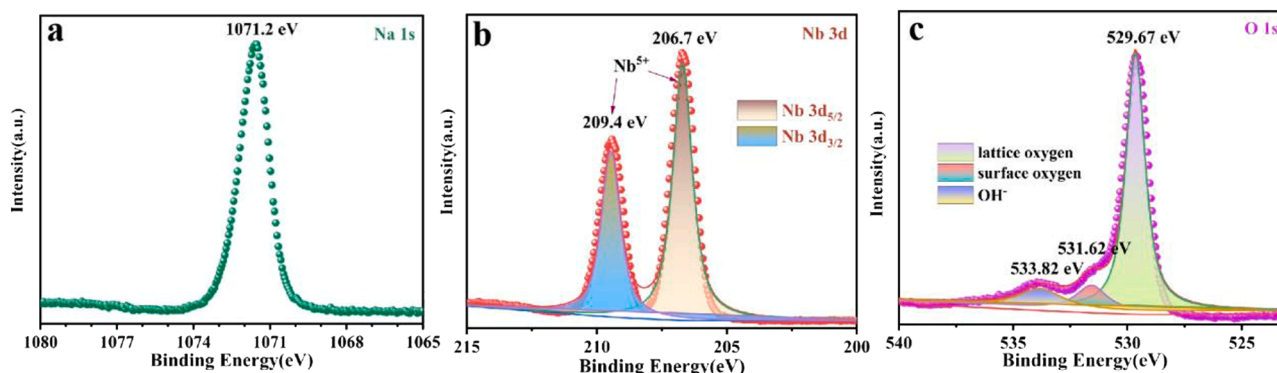$$\eta_{surface} = J_{H2O}/J_{Na2SO3} \tag{4}$$

Fig. 4. XPS spectra of $NaNbO_3$. (a) Na 1 s; (b) Nb 3d; (c) O 1 s.

J_{H2O} and J_{abs} are the measured photocurrent density and the photon absorption expressed as a current density (photocurrent assuming 100 % APCE). J_{Na2SO3} is the photocurrent density measured in the electrolyte with Na_2SO_3 as hole scavenger. From Fig. S7a and b, it can be found that the charge separation efficiency is slightly enhanced. This indicates that the Lorentz force has a positive effect on charge separation, driving slight photogenerated electron-hole pairs to separate.

To verify the contribution of monochromatic light to the current density, the incident photon-to-current conversion efficiency (IPCE) can be calculated using following equation: [45].

$$IPCE = J \frac{hc/e}{\lambda P\text{light}} \tag{5}$$

where hc/e is equal to 1240, J and λ are the photocurrent density (mA/cm^2) and the incident light wavelength (nm), P_{light} is the incident light irradiance (mW/cm^2), respectively. Comparing the data results under the conditions of light and light + magnet in Fig. 10d, the value of IPCE increases from 7.59 % to 8.43 %, but the value of IPCE beyond the intrinsic absorption wavelength is very low, which is also a favorable proof that the magnetic field improves the performance only by enhancing charge separation and transmission. According to the above results, we explain its mechanism from the perspective of electron spin polarization and magnetic coupling theory. Firstly, when slight energy is input or released, the electron spin will flip, that is, from one spin state to another. The transformation of electron spin state can have a positive impact on the performance of water decomposition. Moreover, as a

typical perovskite structure, the transition of electron spin state of $NaNbO_3$ will cause the change of self-occupation rate, which may also be one of the reasons for its performance improvement.

3.3. Magnetic field assisted pyroelectric catalysis of $NaNbO_3$ electrodes

As a perovskite material with both semiconductor and pyroelectric properties, $NaNbO_3$ has unique advantages. Therefore, pyroelectric catalysis is an important part of its application. In this section, the pyroelectric catalysis process with the assistance of a magnetic field is discussed. As shown in Fig. 5a, there is a significant boost in pyroelectric current with the assistance of magnetic field, reaching 0.114 mA/cm^2 at 1.23 V_{RHE}, which is 1.26 times of the original current value. In the process of studying and realizing more efficient hydrogen production by photoelectrode, it is extremely important to obtain considerable photocurrent density under low photocurrent onset and saturation bias. Hence, the applied bias photon-to-current efficiencies (ABPE) was calculated by Eq. (6): [46].

$$ABPE = (J_{Light} - J_{Dark})[(1 \cdot 23 - V_{RHE})/P_{Light}] \tag{6}$$

Here, J_{Light} and J_{Dark} is the photocurrent density under light and dark conditions, V_{RHE} represents the applied potential vs. RHE, and P_{Light} is the intensity of incident light. As shown in Fig. 5d, the pyroelectric catalysis process under the action of a magnetic field, the ABPE of photoanode reaches up to 0.027 % at 0.78 V_{RHE}. In addition, we also compared the influence of magnetic field in pyroelectric catalysis through I-T curve. As shown in Fig. 6b, the influence of Lorentz force on
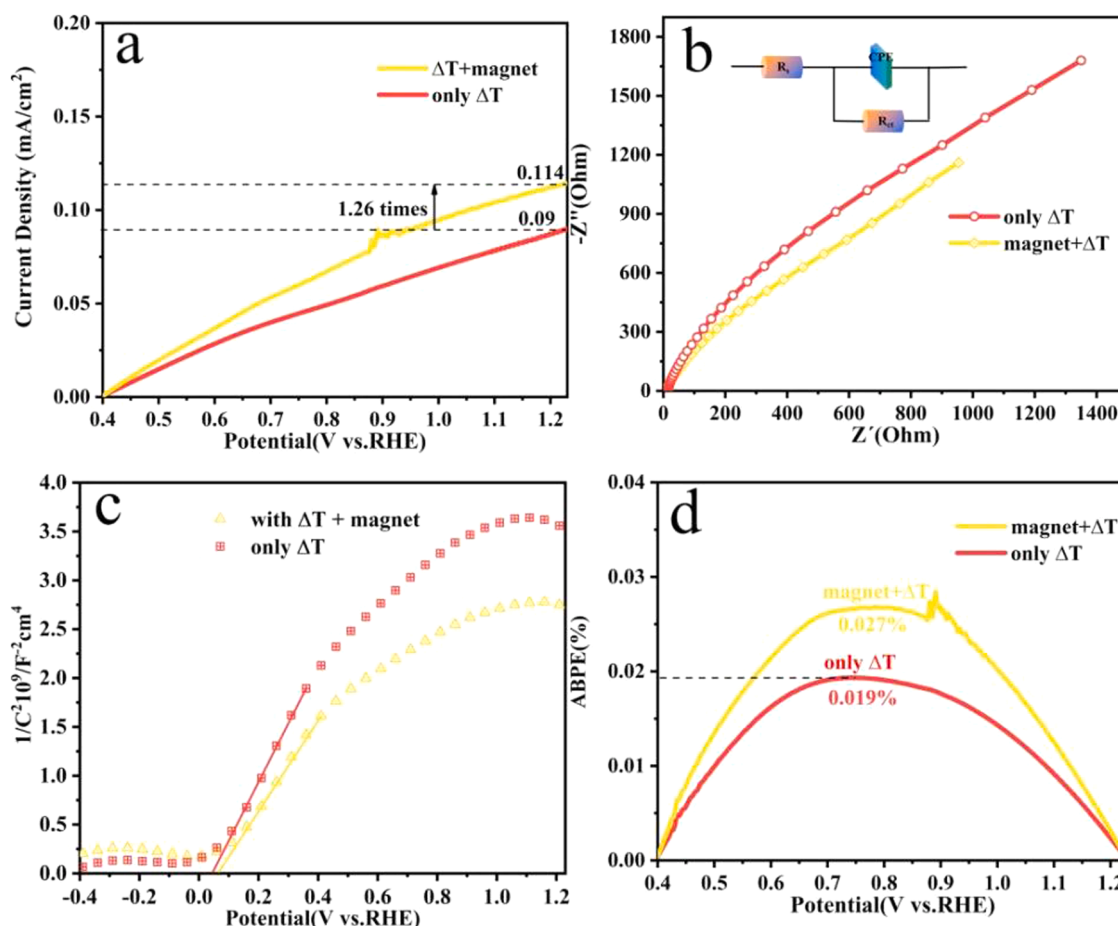

Fig. 5. (a) Current density versus applied potential (I-V) curves of $NaNbO_3$; (b) EIS Nyquist plots of $NaNbO_3$ electrode; (c) Mott-Schottky plots of $NaNbO_3$; (d) ABPE curves of $NaNbO_3$. All the above pyroelectric catalytic tests were carried out in 1.0 M Na_2SO_4 (pH=6.8) electrolyte with the assistance of magnetic field; Embedded graph: the equivalent circuit (where R_s refers to the series resistance, and R_{ct} and CPE are the charge transfer resistance and the constant phase element at the electrode/electrolyte interface, respectively).
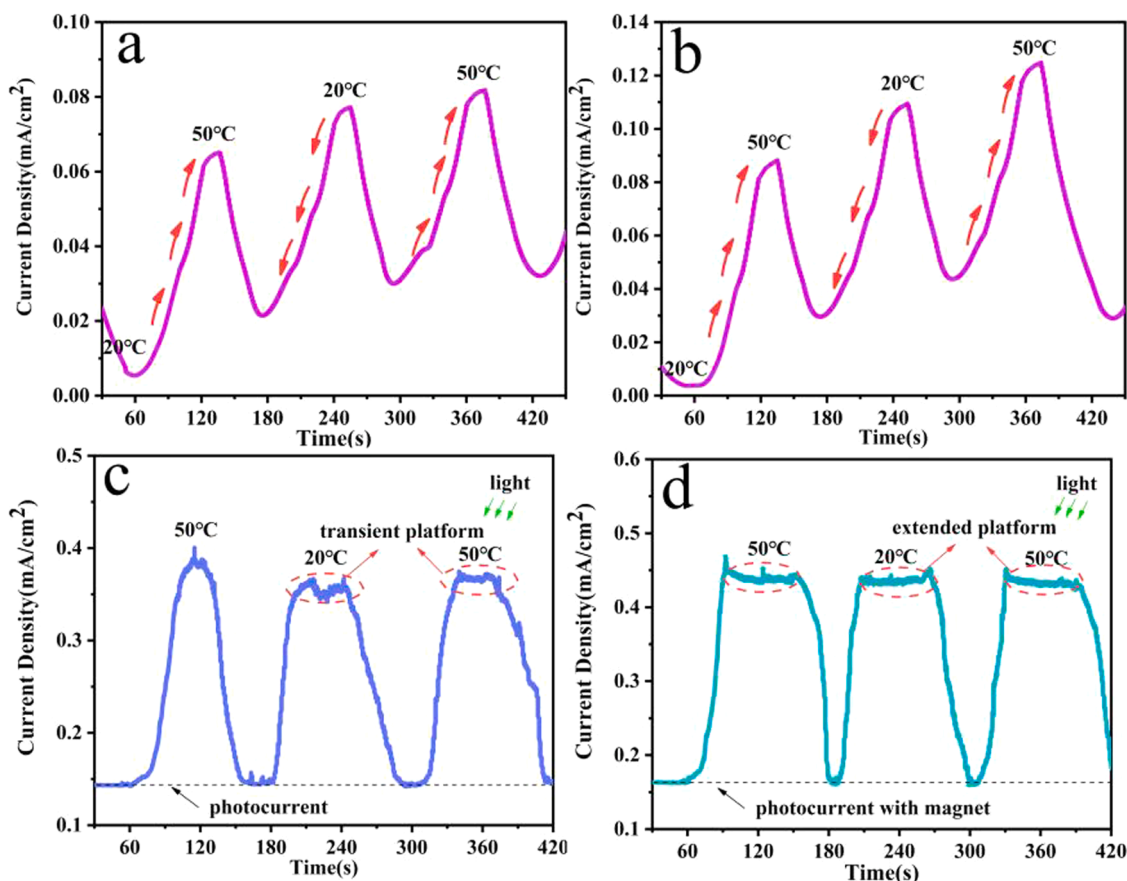
Fig. 6. I-T curve under the different catalytic processes. (a) pyroelectric catalysis; (b) pyroelectric catalysis assisted by magnetic field; (c) pyro-photo-electric catalysis; (d) pyro-photo-electric catalysis assisted by magnetic field.

pyro-generated carriers is significant, and the pyroelectric current increases significantly with the change of temperature. As we all know, structural changes are closely related to performance trends. We calculated the charge density distribution at the two terminal temperatures through the first-principles calculations. As shown in Fig. 7a and b, the charge density distribution of Nb and O atoms in [NbO₆]⁻ octahedron changes significantly with the change of temperature. The temperature rise leads to the change of the inclination of octahedron and the length of Nb-O bond. Obviously, the octahedron changes from a state inclined to the inner cell, the structure tends to be regular, and the length of Nb-O bond increases from 1.90549 Å to 2.13878 Å. The change of structure will cause the change of self-occupation rate, resulting in high catalytic activity [47].

To further elucidate the charge transfer and compounding process of electrodes under the action of magnetic field, the EIS measurements are investigated as presented in Fig. 5b. The equivalent circuit is shown in Fig. 5b, of which R_s represents the series resistance. R_{ct} means charge transfer resistance and CPE refers to the constant phase element. Nyquist plot semicircle arc represents the charge transfer resistance value at electrode-electrolyte interface [48,49]. The pyroelectric catalysis process under the action of a magnetic field exhibits a smaller arc radius than the pyroelectric catalysis alone, demonstrating that the magnetic field accelerates the charge transfer generated by the pyroelectric effect. It is noteworthy that the results of the Mott-Schottky plots show that the magnetic field has little effect on the V_{fb} during the pyroelectric catalysis process and that the magnetic field only leads to a significant increase in the N_d. Specifically, the value of donor density (N_d) is calculated by Eq. (7): [50].

$$N_d = [2/\varepsilon\varepsilon_0 e_0][d(1/C^2)/dV]^{-1} \qquad (7)$$

It is necessary to explain the significant improvement of pyroelectric catalysis performance from the perspective of magnetic field effects. As shown in steps (I) to (II) in Fig. 11, in the state of no temperature change, NaNbO₃ remains in thermodynamic equilibrium and the electric dipole generated by spontaneous polarization is completely shielded by the surface-bound charge. When the crystal is heated/cooled, the decrease/increase in the intensity of spontaneous polarization leads to the release of excess charge on the surface. In the process of pyroelectric catalysis, the external bias and temperature difference will exist at the same time, which leads to the intervention of magnetic field and the emergence of pyro-magnetic effect. Specifically, in the work of the three electrode system, the current direction is x. When the magnetic induction line passes through the sample surface (z direction), a temperature gradient will be generated at both ends of the sample in the y direction. The temperature gradient is proportional to the magnetic induction intensity (B_z) and the current density (J_x), that is:

$$\Delta T = PJ_x B_z. \qquad (8)$$

Here, *P* represents the Ettingshausen coefficient. The temperature gradient at this time is different from the externally applied temperature difference. As shown in steps (II) to (III) in Fig. 11, NaNbO₃ will maintain non thermodynamic equilibrium due to the new temperature gradient, which leads to the release of more charges on the surface. The additional charge release also corroborates the increase in N_d. At the same time, the imbalance of polarization charges and induced pyroelectric potential lead to the change of energy band orientation. This is not only more favorable for the separation and transmission of carriers, but also the reason for the significant increase of pyroelectric catalytic current. We further discussed the change of charge separation efficiency of pyroelectric catalysis assisted by magnetic field. As shown in Fig. S8a
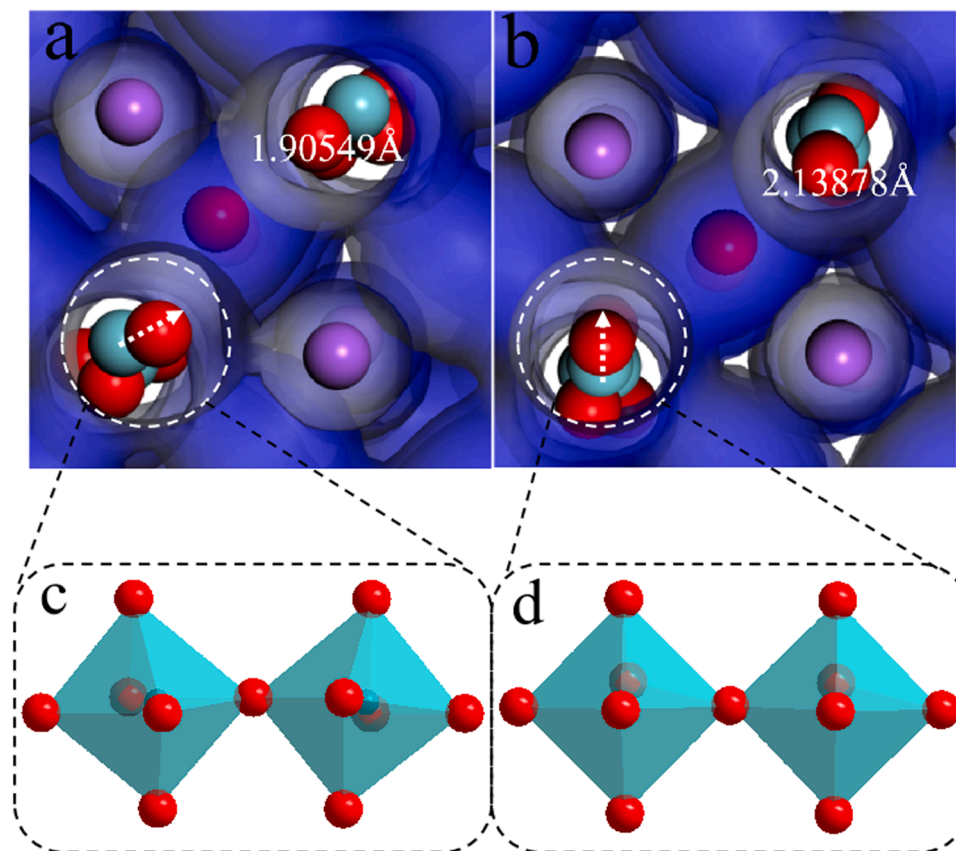
Fig. 7. Charge density distribution of NaNbO$_3$ at different terminal temperatures. (a) 20 ℃; (b) 50 ℃; (c) and (d) are corresponding octahedral structures (purple, cyan and red spheres represent Na, Nb and O atoms, respectively).

and b, under the assistance of a magnetic field, the η_{bulk} and $\eta_{surface}$ of NaNbO$_3$ are 35.9 % and 22.7 % at 1.23 V_{RHE}, respectively, which was significantly higher than only ΔT condition. Bode phase (Fig. S8c) also shows an obviously positive shift from the phase frequency peak to the high-frequency value. The peak value of the phase-angle curve reflects the dynamic properties of interfacial charge transfer over the photo-electrode [51]. The above results show that the magnetic field has a positive impact on the process of pyroelectric catalysis. The magnetic field can not only enhance the charge separation ability through Lorentz force, but also enhance its catalytic performance by using the generated pyro-magnetic effect. To summarize, the magnetic field has a positive and complex effect on the pyroelectric catalytic process: (1) Accelerates the transmission and separation of pyro-generated carriers; (2) The ΔT produced by the magnetic field through the pyro-magnetic effect affects the imbalance between the polarization charge and the induced

potential; (3) Pyro-magnetic effect breaks the limitation of magnetic field controlled carrier non-radiative recombination.

We use COMSOL Multiphysics to simulate the changes of internal temperature and magnetic flux density of NaNbO$_3$ (1 × 1 × 1 μm) under the coupling of external temperature field and magnetic field, so as to more intuitively show the influence mechanism of multi-field coupling. As shown in Fig. 8a and b, it is due to the pyro-magnetic effect that the generation of new temperature gradient leads to unbalanced temperature distribution, which may be the key factor affecting the internal polarization field of NaNbO$_3$. Fig. 8c shows the magnetic flux density distribution in the internal section of the cell, and the external temperature field also affects the magnetic flux density in the cell. The simulation results can explain the relationship between pyro-magnetic effect and pyroelectric effect. The temperature gradient generated by pyro-magnetic effect can affect the internal polarization field of
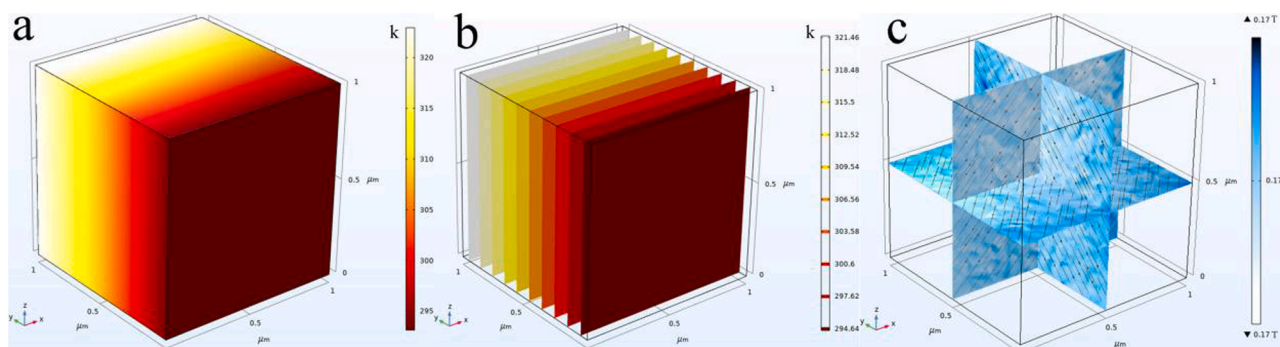

Fig. 8. Coupling of multiple physical fields (magnetic field and thermal field) of NaNbO$_3$ (1 × 1 × 1 μm) simulated by COMSOL. (a) internal temperature distribution; (b) Section distribution of internal temperature; (c) magnetic flux density distribution in internal section.

pyroelectric effect. Correspondingly, the thermal field also affects the magnetic flux density in the cell.

3.4. Magnetic field assisted pyro-photo-electric catalysis of NaNbO$_3$ electrodes

According to the results discussed in Section 3.2, the enhancement of photoelectric performance by magnetic field seems to be limited. We speculate that this may be due to the limitations of non-radiative recombination of Lorentz force manipulating carriers. However, the enhancement of the magnetic field for its pyroelectric catalysis performance is more obvious, which is caused by the presence of the pyromagnetic effect and the effective modulation of the carriers. Considering to this point, we applied the same magnetic field in the pyro-photo-electric system again, and the process is shown in Fig. S5. Also, we compared the tests under different external field conditions, which were used to illustrate the role of the magnetic field. The I-V curves were collected in Fig. 9a. The current density is increased to 0.45 mA/cm^2 at 1.23 V$_{RHE}$ with the assistance of a magnetic field. At the same time, under the ideal temperature rise program, we recorded the I-T curve of pyro-photo-catalysis assisted by magnetic field. Comparing the current changes in Fig. 6c and d, under the action of magnetic field, the growth trend of current with temperature changes has changed significantly, and there is a longer-term stability than the simple pyro-photo-catalysis process. In this process, the magnetic and thermal fields play a joint role and there is a coupling effect between the magnetic and thermal fields. The pyroelectric effect, pyro-magnetic effect and pyro-photo-electric synergies play an active role in the energy band alignment, spin polarization alignment and carrier separation of electrons (as shown in Fig. 11).

Then, electrochemical impedance spectroscopy (EIS) measurements were performed to further explore the charge separation and transfer processes. As expected and in agreement with the results (Fig. 9b), the pyro-photo-electric system under magnetic field assistance has the smallest circle radius and the lowest charge transfer impedance. This suggests that pyro-photo-electric catalysis under magnetic field

assistance exhibits effective carrier transport and suppresses more carrier complexation behavior. In comparing the Mott-Schottky plots under different external field conditions, an increase in donor density is obtained according to Eq. (7). Detailed calculation results are shown in Tab. S1. The depletion width (W_{dep}) can be estimated based on the following equation to evaluate the characteristics of the sample at the electrode/electrolyte interface: [52]

$$W dep = \left[\frac{2\varepsilon_0\varepsilon(V - Vfb)}{qNd} \right]^{1/2} \tag{9}$$

Interestingly, pyroelectric effect and pyro-magnetic effect are the key to the negative shift of V_{fb}, which indicates that the change of energy band bending degree and W_{dep} are also part of the factors to improve the performance. The detailed value of the W_{dep} under the condition of multi-field coupling is shown in the Fig. 10b. At 1.23 V$_{RHE}$, the W_{dep} is reduced to 34.7 nm, which will shorten the charge collection distance [53,54]. Therefore, holes will participate in the electrode water oxidation process with higher probability. Correspondingly, the ABPE value of the pyro-photo-electric system with magnetic field assistance is 0.14 % at a bias voltage of 0.72 V$_{RHE}$, both significantly higher than the ABPE values under other conditions. In detail, the measurement results of charge separation efficiency are shown in Fig. 9e-f. The introduction of magnetic field in the process of pyro-photo-electric system can significantly improve its charge separation efficiency, and its η_{bulk} and $\eta_{surface}$ reach 65.4 % and 55.9 % respectively. The significant high frequency shift of Bode phase diagram (Fig. 10a) also means that it is a process of rapid carrier transport. From the Tafel slopes derived from the I-V curves for OER (Fig. 10c), we can see that the sample under the light + magnet + ΔT (74.9 mV dec^{-1}) condition has the lowest Tafel slope value than that of the light + ΔT (92.3 mV dec^{-1}), the light + magnet (123.9 mV dec^{-1}), the magnet + ΔT (174.3 mV dec^{-1}). The coupling of multiple fields (magnetic field and temperature field) is significant for the gain of photoelectric catalysis process, which also proves that the coupling relationship between pyro-magnetic effect and pyroelectric effect can be realized in photoelectric catalysis. The non-radiative recombination regulation of carriers by pyro-magnetic effect is tally with the built-in
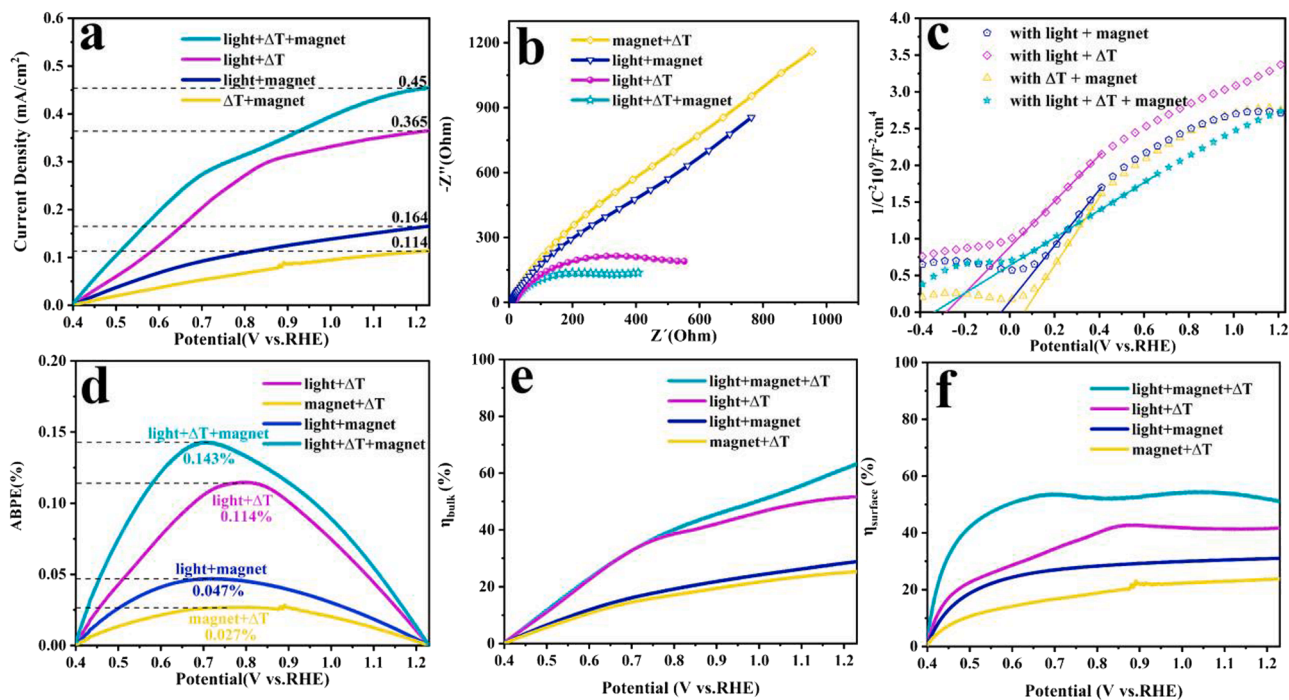

Fig. 9. (a) Current density versus applied potential (I-V) curves of NaNbO$_3$; (b) EIS Nyquist plots of NaNbO$_3$ electrode; (c) Mott-Schottky plots collected at a fixed frequency of 1 kHz; (d) ABPE curves of NaNbO$_3$. (e, f) The charge separation efficiency of NaNbO$_3$. All the above measurements are carried out with the different external field conditions.
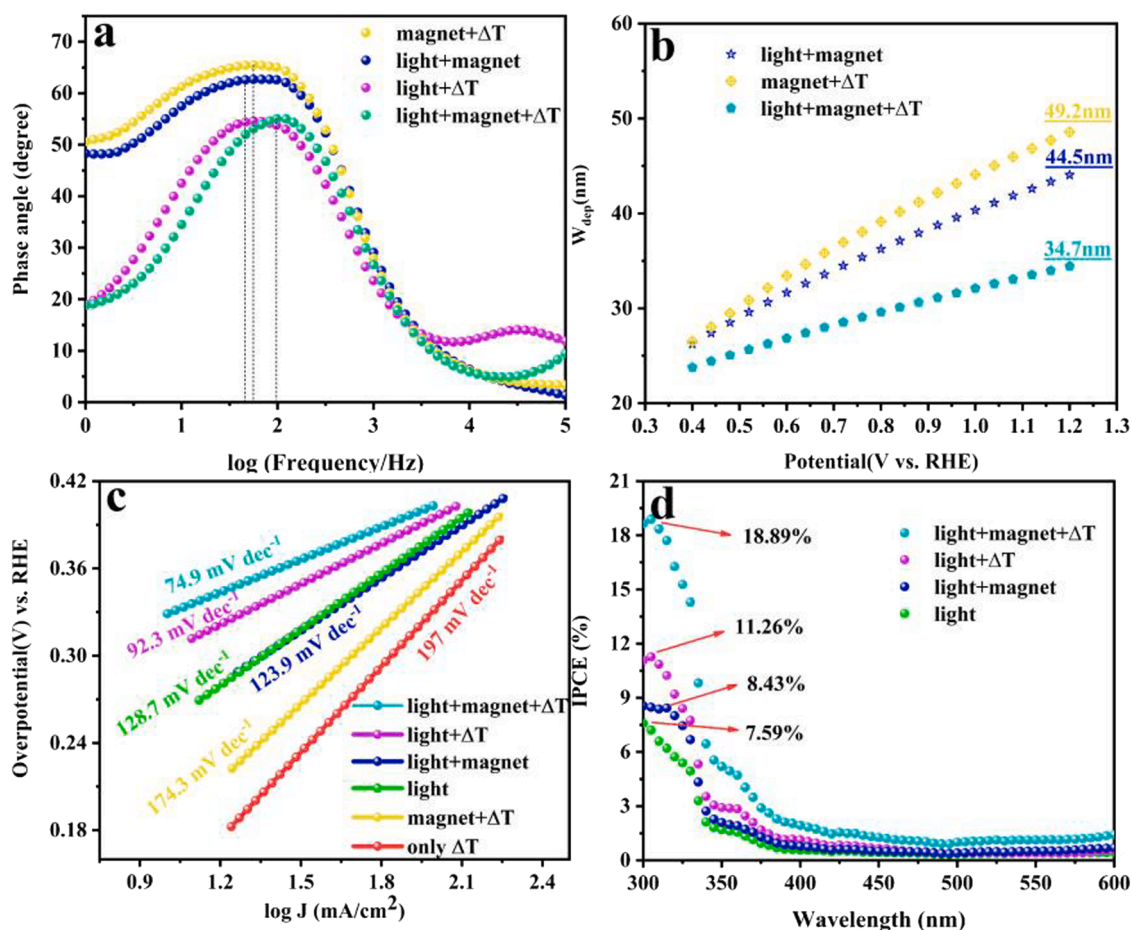
Fig. 10. (a) Bode phase plots of the NaNbO₃; (b) The diagram of W_{dep} under different applied voltages in magnetic field assisted pyro-photo-electric catalysis; (c) The tafel plots derived from LSV curves; (d) IPCE spectra collected at the incident wavelength range from 300 to 600 nm at 1.23 V vs. RHE of NaNbO₃.
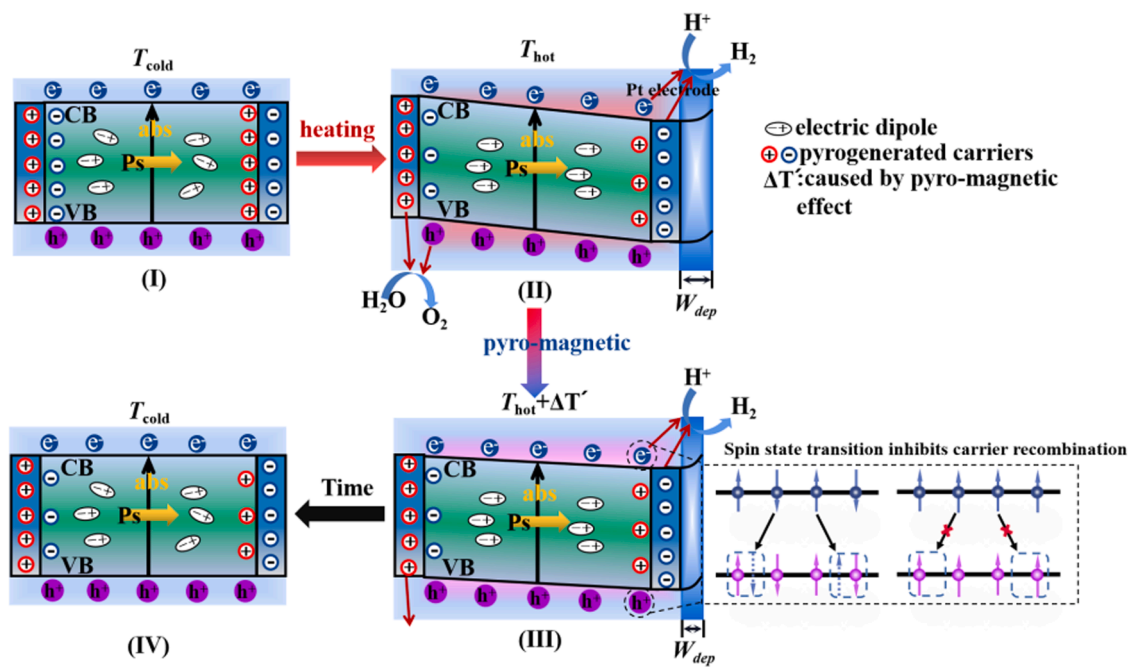

Fig. 11. The mechanism of pyroelectric and pyro-magnetic effects in catalytic process.

electric field provided by pyroelectric effect to enhance carrier separation. As shown in the Tab. S2, we summarize the catalytic activity and performance evaluation of different semiconductor materials under external field assistance, in comparison, our proposed multi-field coupled-assisted photoelectric catalysis process exhibits excellent catalytic activity. The high efficiency of incident photon-to-current conversion is also an important prerequisite for PEC water splitting. The incident photon-to-currentt conversion efficiency (IPCE) measurement is used to evaluate the contribution of monochromatic light to photocurrent. Therefore, as shown in Fig. 10d, compared with other conditions, the photoanode shows the highest IPCE value under the condition of multi-field coupling, reaching about 18.89 %. Moreover, the IPCE value is consistent with the I-V curves result.

4. Conclusion

In conclusion, we use $NaNbO_3$ semiconductor with non-centrosymmetric central structure to study the effect of magnetic field on photoelectric and pyroelectric catalysis respectively. The experimental results show that the enhancement of magnetic field on photoelectric performance seems to be limited. We believe that this is due to the limitation of non-radiative recombination of carriers manipulated by Lorentz force. The pyroelectric catalytic performance improved significantly with the help of magnetic field, and the pyroelectric current increased to 0.11 mA/cm^2 at 1.23 V_{RHE} (upgrade 1.26 times). This is not only because the pyro-magnetic effect breaks through the limitation of non-radiative recombination regulation of carriers, but also because the magnetic field controls more carrier separation. The results of DFT calculation and COMSOL simulation also illustrate the connection and interaction mechanism of multi-physical field coupling (magnetic field and temperature field). Finally, we explored the synergistic photoelectric of magnetic and thermal field to further improve the water splitting performance of the electrode. Under the combined action of magnetic field and temperature field, the current density of photoanode reaches 0.45 mA/cm^2 at 1.23 V_{RHE} (3 times higher than photocurrent). Through experimental measurement and analysis, the interaction mechanism between pyro-magnetic and pyroelectric effect is revealed, which not only provides ideas for the effective utilization of magnetic field in the field of pyroelectric catalysis, but also provides insights for the application of multi field coupling assisted PEC.

CRediT authorship contribution statement

Zhifeng Liu and **Tianhao Li** conceived and designed the study. **Tianhao Li** performed the experiments. **Zhifeng Liu, Tianhao Li** and **Yongjin Zou** wrote the paper. **Zhifeng Liu, Tianhao Li** and **Yongjin Zou** reviewed and edited the manuscript. All authors read and approved the manuscript.

Declaration of Competing Interest

The authors declare that they have no known competing financial interests or personal relationships that could have appeared to influence the work reported in this paper.

Data availability

Data will be made available on request.

Acknowledgements

Appendix A. Supporting information

Supplementary data associated with this article can be found in the online version at doi:10.1016/j.apcatb.2023.122486.

References

[1] I. Roger, M.A. Shipman, M.D. Symes, Earth-abundant catalysts for electrochemical and photoelectrochemical water splitting, Nat. Rev. Chem. 1 (2017) 1–13.

[2] X. Du, J. Huang, J. Zhang, Y. Yan, C. Wu, Y. Hu, C. Yan, T. Lei, W. Chen, C. Fan, J. Xiong, Modulating electronic structures of inorganic nanomaterials for efficient electrocatalytic water splitting, Angew. Chem. Int. Ed. 58 (2019) 4484–4502.

[3] Xiaomeng Zhang, Panlong Zhai, Yanxue Zhang, Yunzhen Wu, Chen Wang, Lei Ran, Junfeng Gao, Zhuwei Li, Bo Zhang, Zhaozhong Fan, Licheng Sun, Jungang Hou, Engineering single-atomic Ni-N$_4$-O sites on semiconductor photoanodes for high-performance photoelectrochemical water splitting, J. Am. Chem. Soc. 143 (2021) 20657–20669.

[4] Lei Ran, Shi Qiu, Panlong Zhai, Zhuwei Li, Junfeng Gao, Xiaomeng Zhang, Bo Zhang, Chen Wang, Licheng Sun, Jungang Hou, Conformal macroporous inverse opal oxynitride-based photoanode for robust photoelectrochemical water splitting, J. Am. Chem. Soc. 143 (2021) 7402–7413.

[5] Y. Lee, J. Suntivich, K.J. May, E.E. Perry, Y. Shao-Horn, Synthesis and activities of rutile IrO$_2$ and RuO$_2$ nanoparticles for oxygen evolution in acid and alkaline solutions, J. Phys. Chem. Lett. 3 (2012) 399–404.

[6] H. Wang, Z. Chen, D. Wu, M. Cao, F. Sun, H. Zhang, H. You, W. Zhuang, R. Cao, Significantly enhanced overall water splitting performance by partial oxidation of Ir through Au modification in core-shell alloy structure, J. Am. Chem. Soc. 143 (2021) 4639–4645.

[7] S. Cherevko, S. Geiger, O. Kasian, N. Kulyk, J.P. Grote, A. Savan, B.R. Shrestha, S. Merzlikin, B. Breitbach, A. Ludwig, K.J.J. Mayrhofer, Oxygen and hydrogen evolution reactions on Ru, RuO$_2$, Ir, and IrO$_2$ thin film electrodes in acidic and alkaline electrolytes: a comparative study on activity and stability, Catal. Today 262 (2016) 170–180.

[8] K.S. Exner, J. Anton, T. Jacob, H. Over, Ligand effects and their impact on electrocatalytic processes exemplified with the oxygen evolution reaction (OER) on RuO$_2$ (110), ChemElectroChem 2 (2015) 707–713.

[9] Y. Hu, G. Luo, L. Wang, X. Liu, Y. Qu, Y. Zhou, F. Zhou, Z. Li, Y. Li, T. Yao, C. Xiong, B. Yang, Z. Yu, Y. Wu, Single Ru atoms stabilized by hybrid amorphous/crystalline FeCoNi layered double hydroxide for ultraefficient oxygen evolution, Adv. Energy Mater. 11 (2021), 2002816.

[10] Y. Zhang, Y. Lei, T. Zhu, Z. Li, S. Xu, J. Huang, X. Li, W. Cai, Y. Lai, X. Bao, Surface plasmon resonance metal-coupled biomass carbon modified TiO$_2$ nanorods for photoelectrochemical water splitting, Chin. J. Chem. Eng. 41 (2022) 403–411.

[11] N. Le, N.T.N. Truong, N.H. Lam, A.M. Tamboli, S.S. Patil, M.S. Tamboli, J.H. Jung, Enhanced light absorption and charge separation of In-doped ZnO nanorod arrays for photoelectrochemical water-splitting application, Int. J. Energy Res. 46 (2022) 6264–6276.

[12] D. Chen, Z. Liu, Z. Guo, M. Ruan, W. Yan, 3D branched Ca-Fe$_2$O$_3$/Fe$_2$O$_3$ decorated with Pt and Co-Pi: improved charge-separation dynamics and photoelectrochemical performance, ChemSusChem 12 (2019) 3286–3295.

[13] S. Wang, C. Meng, Y. Bai, Y. Wang, P. Liu, L. Pan, L. Zhang, Z. Yin, N. Tang, Synergy promotion of elemental doping and oxygen vacancies in Fe$_2$O$_3$ nanorods for photoelectrochemical water splitting, ACS Appl. Nano Mater. 5 (2022) 6781–6791.

[14] G. Fang, Z. Liu, C. Han, Enhancing the PEC water splitting performance of BiVO$_4$ co-modifying with NiFeOOH and Co-Pi double layer cocatalysts, Appl. Surf. Sci. 515 (2020) 146095.

[15] S.G. Shim, J. Tan, H. Lee, J. Park, J. Yun, S.Y. Park, K. Kim, J. Lee, J. Moon, Facile morphology control strategy to enhance charge separation efficiency of Mo: BiVO$_4$ photoanodes for efficient photoelectrochemical water splitting, Chem. Eng. J. 430 (2022), 133061.

[16] Q. Zhao, Z. Liu, Z. Guo, M. Ruan, W. Yan, The collaborative mechanism of surface S-vacancies and piezoelectric polarization for boosting CdS photoelectrochemical performance, Chem. Eng. J. 433 (2022) 133226.

[17] L. Wei, J. Zhang, M. Ruan, Combined CdS/In$_2$S$_3$ heterostructures with cocatalyst for boosting carriers separation and photoelectrochemical water splitting, Appl. Surf. Sci. 541 (2021) 148431.

[18] S. Zhang, D. Chen, Z. Liu, M. Ruan, Z. Guo, Novel strategy for efficient water splitting through pyro-electric and pyro-photo-electric catalysis of BaTiO$_3$ by using thermal resource and solar energy, Appl. Catal. B Environ. 284 (2021) 119686.

[19] Q. Zhao, Z. Liu, J. Li, W. Yan, J. Ya, X. Wu, Piezoelectric polarization assisted WO$_3$/CdS photoanode improved carrier separation efficiency via CdS phase regulation, Int. J. Hydrog. Energy 46 (2021) 36113–36123.

[20] T. Li, Z. Guo, M. Ruan, Y. Zou, Z. Liu, Doping regulating spontaneous polarization and pyroelectric effects to synergistically promote the water splitting efficiency of niobate (K$_x$Na$_{1-x}$NbO$_3$) pyro-photo-electrical coupling system, Appl. Surf. Sci. 592 (2022) 153255.

[21] J. Li, Q. Pei, R. Wang, Y. Zhou, Z. Zhang, Q. Cao, Y. Du, Enhanced photocatalytic performance through magnetic field boosting carrier transport, ACS Nano 12 (2018) 3351–3359.

[22] W. Gao, Q. Liu, S. Zhang, Y. Yang, X. Zhang, H. Zhao, Y. Sang, Electromagnetic induction derived micro-electric potential in metal-semiconductor core-shell hybrid nanostructure enhancing charge separation for high performance photocatalysis, Nano Energy 71 (2020), 104624.

[23] M. Wang, B. Wang, F. Huang, Z. Lin, Enabling PIEZOpotential in PIEZOelectric semiconductors for enhanced catalytic activities, Angew. Chem. Int. Ed. 58 (2019) 7526–7536.

[24] S. Zhang, Z. Liu, M. Ruan, Z. Guo, E. Lei, W. Zhao, D. Chen, Enhanced piezoelectric-effect-assisted photoelectrochemical performance in ZnO modified with dual cocatalysts, Appl. Catal. B Environ. 262 (2020), 118279.

[25] Z. Qiao, Z. Liu, W. Yan, M. Ruan, Z. Guo, X. Wu, Pyro-photo-electric catalysis in Bi_2WO_6 nanostructures for efficient degradation of dyes under thermal-assisted visible light irradiation, J. Alloy. Compd. 892 (2022), 162203.

[26] H. You, Z. Wu, L. Wang, Y. Jia, S. Li, J. Zou, Highly efficient pyrocatalysis of pyroelectric $NaNbO_3$ shape-controllable nanoparticles for room-temperature dye decomposition, Chemosphere 199 (2018) 531–-537.

[27] L. Jiang, Y. Qiu, Z. Yi, Potassium niobate nanostructures: controllable morphology, growth mechanism, and photocatalytic activity, J. Mater. Chem. A 1 (2013) 2878–2885.

[28] A.D. Handoko, G.K.L. Goh, Hydrothermal synthesis of sodium potassium niobate solid solutions at 200℃, Green Chem. 12 (2010) 680–687.

[29] F. Zhang, L. Han, S. Bai, T. Sun, T. Karaki, M. Adachi, Hydrothermal synthesis of (K, Na) NbO_3 particles, Jpn. J. Appl. Phys. 47 (2008) 7685.

[30] Y. Xu, Q. Yu, J. Li, A facile method to fabricate vertically aligned (K, Na) NbO_3 lead-free piezoelectric nanorods, J. Mater. Chem. 22 (2012) 23221–23226.

[31] S. Zhang, B. Zhang, D. Chen, Z. Guo, M. Ruan, Z. Liu, Promising pyro-photo-electric catalysis in $NaNbO_3$ via integrating solar and cold-hot alternation energy in pyroelectric-assisted photoelectrochemical system, Nano Energy 79 (2021), 105485.

[32] Q. Yang, J. Du, X. Nie, D. Yang, L. Bian, L. Yang, F. Dong, H. He, Y. Zhou, H. Yang, Magnetic field-assisted photoelectrochemical water splitting: the photoelectrodes have weaker nonradiative recombination of carrier, ACS Catal. 11 (2021) 1242–1247.

[33] S.S. Kalanur, R. Singh, H. Seo, Enhanced solar water splitting of an ideally doped and work function tuned {002} oriented one-dimensional WO_3 with nanoscale surface charge mapping insights, Appl. Catal. B Environ. 295 (2021), 120269.

[34] P. Li, S. Ouyang, G. Xi, T. Kako, J. Ye, The effects of crystal structure and electronic structure on photocatalytic H_2 evolution and CO_2 reduction over two phases of perovskite-structured $NaNbO_3$, J. Phys. Chem. C 116 (2012) 7621–7628.

[35] L. Pan, M. Ai, C. Huang, L. Yin, X. Liu, R. Zhang, S. Wang, Z. Jiang, X. Zhang, J. J. Zou, W. Mi, Manipulating spin polarization of titanium dioxide for efficient photocatalysis, Nat. Commun. 11 (2020) 1–9.

[36] P. Chen, W. Zhou, H. Zhang, Q. Pan, X. Zhang, B. Chu, Large thermal-electrical response and rectifying conduction behavior in asymmetrically reduced ferroelectric ceramics, ACS Appl. Electron. Mater. 1 (2019) 478–484.

[37] J. Lee, A. Kumar, M.G. Kim, T. Yang, X. Shao, X. Liu, H. Lee, Single-metal-atom dopants increase the lewis acidity of metal oxides and promote nitrogen fixation, ACS Energy Lett. 6 (2021) 4299–4308.

[38] H. Yan, X. Wang, X. Yao M, Yao. Band structure design of semiconductors for enhanced photocatalytic activity: the case of TiO_2, Prog. Nat. Sci. Mater. Int. 23 (2013) 402–407.

[39] X. Yan, G. Li, Z. Yu, G. Liu, C. Yang, J. Hu, K. Wang, Advances in magnetic-field assisted photoelectrochemical systems for highly efficient conversion of renewable energy, Adv. Mater. Interfaces 8 (2021), 2100446.

[40] X. Li, W. Wang, F. Dong, Z. Zhang, L. Han, X. Luo, T. Zhang, Recent advances in noncontact external-field-assisted photocatalysis: from fundamentals to applications, ACS Catal. 11 (2021) 4739–4769.

[41] Q. Luan, X. Xue, R. Li, L. Gu, W. Dong, D. Zhou, C. Hou, Boosting photocatalytic hydrogen evolution: orbital redistribution of ultrathin $ZnIn_2S_4$ nanosheets via atomic defects, Appl. Catal. B Environ. 305 (2022), 121007.

[42] K.H. Ye, Z. Wang, J. Gu, S. Xiao, Y. Yuan, Y. Zhu, Y. Zhang, W. Mai, S. Yang, Carbon quantum dots as a visible light sensitizer to significantly increase the solar water splitting performance of bismuth vanadate photoanodes, Energy Environ. Sci. 10 (2017) 772–779.

[43] H. Dotan, K. Sivula, M. Gr-tzel, A. Rothschild, S.C. Warren, Energy Environ. Sci. 4 (2011) 958–964.

[44] D. Chen, Z. Liu, Dual-axial gradient doping (Zr and Sn) on hematite for promoting charge separation in photoelectrochemical water splitting, ChemSusChem 11 (2018) 3438–3448.

[45] Y. Han, J. Wu, Y. Li, X. Gu, T. He, Y. Zhao, Z. Kang, Carbon dots enhance the interface electron transfer and photoelectrochemical kinetics in TiO_2 photoanode, Appl. Catal. B Environ. 304 (2022), 120983.

[46] H. Chai, L. Gao, P. Wang, F. Li, G. Hu, J. Jin, In_2S_3/F-Fe_2O_3 type-II heterojunction bonded by interfacial SO for enhanced charge separation and transport in photoelectrochemical water oxidation, Appl. Catal. B Environ. 305 (2022), 121011.

[47] Y. Tong, Y. Guo, P. Chen, H. Liu, M. Zhang, L. Zhang, W. Yan, W. Chu, C. Wu, Y. Xie, Spin-state regulation of perovskite cobaltite to realize enhanced oxygen evolution activity, Chem 3 (2017) 812–821.

[48] B. Klahr, S. Gimenez, F. Fabregat-Santiago, T. Hamann, J. Bisquert, Water oxidation at hematite photoelectrodes: the role of surface states, J. Am. Chem. Soc. 134 (2012) 4294–4302.

[49] N. Li, Y. Jiang, X. Wang, C. Hu, W. Jiang, S. Li, L. Xia, Efficient charge separation and transfer of a TaON/$BiVO_4$ heterojunction for photoelectrochemical water splitting, RSC Adv. 11 (2021) 13269–13273.

[50] K. Wang, Y. Li, L. Li, C. Wang, Y. Fang, W. Zhao, F. Jian, Efficient carrier transfer route via the bridge of C_{60} particle to TiO_2 nanoball based coverage layer enables stable and efficient cadmium free GeSe photocathode for solar hydrogen evolution, Appl. Catal. B Environ. 297 (2021), 120437.

[51] B. Baral, D.P. Sahoo, K. Parida, Discriminatory {040}-reduction facet/Ag^0 schottky barrier coupled {040/110}-$BiVO_4$@ Ag@CoAl-LDH Z-scheme isotype heterostructure, Inorg. Chem. 60 (2021) 1698–1715.

[52] A. Kuila, P. Saravanan, D. Bahnemann, C. Wang, Novel Ag decorated, BiOCl surface doped $AgVO_3$ nanobelt ternary composite with Z-scheme homojunction-heterojunction interface for high prolific photo switching, quantum efficiency and hole mediated photocatalysis, Appl. Catal. B Environ. 293 (2021), 120224.

[53] Z. Zhang, H. Nagashima, T. Tachikawa, Ultra-narrow depletion layers in a hematite mesocrystal-based photoanode for boosting multihole water oxidation, Angew. Chem. Int. Ed. 59 (2020) 9047–9054.

[54] C. Li, A. Li, Z. Luo, J. Zhang, X. Chang, Z. Huang, T. Wang, J. Gong, Surviving high-temperature calcination: ZrO_2-induced hematite nanotubes for photoelectrochemical water oxidation, Angew. Chem. 129 (2017) 4214–4219.